Nanoscale Advances

ROYAL SOCIETY OF CHEMISTRY

PAPER

View Article Online
View Journal | View Issue

Cite this: *Nanoscale Adv.*, 2022, **4**, 1445

Bio-inspired hierarchical nanoporous carbon derived from water spinach for high-performance supercapacitor electrode materials†

Xinyu Lin,‡[a] Yaping Xu,‡[a] Jinggao Wu*[b] and Jing Huang *[a]

Due to various properties, green carbon nanomaterials with high specific surface area and environmentally friendly features have aroused extensive interest in energy storage device applications. Here, we report a facile, one-step carbonization of water spinach to synthesize porous carbon that exhibits a high specific surface area of ~1559 m^2 g^{-1}, high specific capacitance (~1191 F g^{-1} at 1 A g^{-1}), a low intercept (0.9 Ω), outstanding rate capability and superior cycling stability (94.3% capacitance retention after 10 000 cycles). Moreover, the assembled symmetric cell delivers a high energy density of ~85 W h kg^{-1} at 1200 W kg^{-1} and ultra-high stability (loss of 6.8% after 10 000 cycles). An energy density of 49 W h kg^{-1} could also be achieved even with a power density of up to 24 kW kg^{-1}, which indicates that this material could be a promising candidate for future applications in aqueous-based supercapacitors.

Received 20th August 2021
Accepted 22nd January 2022

DOI: 10.1039/d1na00636c

rsc.li/nanoscale-advances

1. Introduction

Due to their high specific power and long cycle life, supercapacitors, including electrochemical double-layer capacitors (EDLCs) and pseudocapacitors, have been deemed promising alternatives or complements for high-power apparatus.[1–3] Concerning supercapacitors, it is important to explore and develop electrode materials with high performance. In general, the materials for supercapacitor devices usually have the basic characteristics of a wide range of sources, low cost and environmentally friendly synthesis methods.[4–8] Meanwhile, a superior electrochemical capacitor electrode material should also have a graded polyporous structure, including macropores, mesoporous pores, and micropores. It is found that the microstructures of carbon materials obtained by carbonization are largely dependent on their precursors.[9–12]

Supercapacitor electrode materials come from a wide range of sources, from non-renewable petroleum and mineral products and their derivatives (*e.g.*, coal, coke, asphalt and synthetic organic polymers) to renewable natural products and their derivatives (*e.g.*, corn cobs, fungi, wood sawdust, banana peels and fish scales).[13–20] Consequently, biomass, which is an environmentally friendly renewable resource, has been suggested as a raw material for the production of specific carbon-based substances. Biomass is readily sourced, inexpensive and easily modified; therefore, replacing nonrenewable petroleum-based materials with biomass in a wide range of applications could effectively alleviate resource shortages and environmental pollution. These factors could contribute to biomass with high carbon content as an attractive raw material for the preparation of advanced functional carbon materials.[21–24]

Water spinach is a crude, fiber-rich, hollow and porous vegetable that is widely cultivated in China. Moreover, the stem of water spinach consists of compounds such as proteins, carbohydrates, lipids, phenols, terpenes, triterpenoids, and

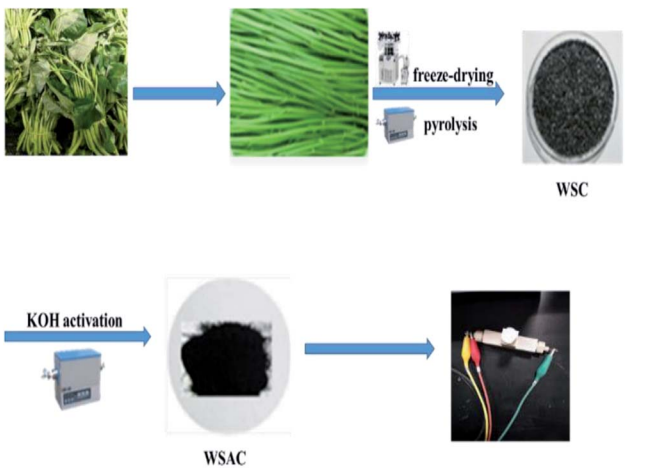

Scheme 1 Synthetic procedure to obtain porous carbon from water spinach.

[a]State Key Laboratory of Silkworm Genome Biology, Key Laboratory of Sericultural Biology and Genetic Breeding, Ministry of Agriculture and Rural Affairs, College of Sericulture, Textile and Biomass Sciences, Southwest University, Chongqing 400715, P. R. China. E-mail: hj41012@163.com

[b]Key Laboratory of Rare Earth Optoelectronic Materials & Devices, College of Chemistry and Materials Engineering, Huaihua University, Huaihua 418000, P. R. China

† Electronic supplementary information (ESI) available. See DOI: 10.1039/d1na00636c

‡ Equal contribution to this work.

carotenoids. In this context, we have developed a novel strategy to prepare porous carbon with water spinach as a raw material by freeze-drying, pyrolysis in argon, and KOH activation to maximize the economic value of water spinach (Scheme 1). By optimizing the carbonization temperature and the mass ratio of coarse carbon and KOH, the porosity and capacitance have been balanced. The structure–activity relationship between the structure and the performance of the resulting porous carbon as well as the energy storage mechanism of the supercapacitor are also further investigated in detail.

2. Experimental section

2.1 Materials and methods

2.1.1 Materials and reagents. Water spinach was collected from a vegetable market in Chongqing, China, and the water spinach sticks were collected after removing the sludge and refreezing. Nafion solution, poly(tetrafluoroethylene) (PTFE), and acetylene black were purchased from Sigma-Aldrich. Potassium hydroxide (KOH) and all other reagents were obtained from Adamas-beta®. All chemicals were used without further purification.

2.1.2 Preparation of water spinach-derived activated carbon (WSAC). Activated carbon was prepared by pyrolysis using water spinach and KOH as raw materials. Firstly, the water spinach was heated in a tubular furnace under argon atmosphere to 600 °C with a heating rate of 5 °C min^{-1}, and it was cooled to room temperature after 3 hours of heat preservation. The obtained carbon was named WSC. Secondly, WSC and KOH with a mass ratio of 1 : 1 were thoroughly ground in an agate mortar. After grinding, the mixture was further heated to 800 °C according to a similar pyrolysis process of WSC in a tube furnace. Finally, the obtained carbon was named WSAC-3. For comparison, different mass ratios of WSC and KOH (2 : 1; 3 : 2, 1 : 1.5, 1 : 2) were also investigated under the above process. The samples were denoted as WSAC-1, WSAC-2, WSAC-4 and WSAC-5. In addition, WSAC-6, WSAC-7 and WSAC-8 were prepared at 600, 700 and 900 °C in accordance with a similar procedure to WSAC-3. In the whole process, all carbonized samples were neutralized with diluted HCl, washed with deionized water, and then dried at 80 °C for 12 h.

2.2 Characterizations

The XRD patterns of all samples were recorded using powder X-ray diffraction (Shimadzu XRD-7000). The surface morphologies and structures of the samples were observed using scanning electron microscopy (FESEM, JSM-7800F) and transmission electron microscopy (TEM, JEOL 2100). Nitrogen sorption isotherms were obtained using an Autosorb-1 (Quantachrome Instruments). The specific surface area was calculated by the modified Brunauer–Emmet–Teller (BET) method. The pore size distributions and the pore volumes were analyzed from the adsorption branch isotherms by density functional theory (DFT). Moreover, the total pore volumes (V_t) were estimated from the amount adsorbed at a relative pressure P/P_0 of 0.990. The micropore volumes (V_{mic}) and micropore surface areas (S_{mic}) were determined by the *t*-plot theory. Raman spectra were acquired with a Jobin-Yvon HR 800 spectrometer. X-ray photoelectron spectroscopy (XPS) measurements were performed on a Thermo Fisher Scientific (Escalab 250xi, USA). Fourier transform infrared (FT-IR) spectra were recorded on a Thermo Scientific Nicolet iS 50 spectrometer.

2.3 Electrochemical measurements

For the two-electrode system, a homogeneous slurry of the electroactive material, polytetrafluoroethylene (PTFE), and acetylene black with a weight ratio of 80 : 10 : 10 in ethanol was formed and pasted to the nickel foam current collector (1 cm × 1 cm), then vacuum dried at 80 °C for 12 h. The loading of the active material for each working electrode was measured to be ~3 mg cm^{-2}. Then, a glass-fiber filter paper (Waterman, GF/B) as a separator and 1 M KOH aqueous solution as the electrolyte were used to assemble a test cell. For the three-electrode system, the working electrode was manufactured *via* the dispersion of active carbon in a mixture of Nafion and ethanol (1 : 20) dropped on glassy carbon electrode, accompanied by platinum foil and Hg/HgO as the counter and reference electrodes, respectively. Electrochemical characterization was carried out on an electrochemical workstation (Shanghai Chenhua Instrument Co. Ltd, China).

For the two-electrode system, the gravimetric specific capacitance of a single electrode is calculated by the equation:

$$C_{sp} = 2I \times \Delta t/m \times \Delta V \quad (1)$$

where C_{sp} (F g^{-1}) is the specific capacitance based on the mass of the active carbons, I is the discharge current (A), Δt is the discharge time (s), ΔV is the voltage difference (except for the ohm drop) within Δt (V), and m is the loading of the active material in each working electrode (g).

For the three-electrode system, the gravimetric specific capacitance can be calculated by the following equations:

$$C_{sp} = I \times \Delta t/m \times \Delta V \quad (2)$$

where I is the discharge current (A), Δt is the discharge time (s), ΔV is the voltage (V), and m is the mass of the active materials (g).

The energy density E (W h kg^{-1}) and the power density P (W kg^{-1}) were calculated by the following equations:

$$E = C_{sp}V^2/(2 \times 3.6) \quad (3)$$

$$P = 3600E/\Delta t \quad (4)$$

where t is the discharge time (s).

3. Results and discussion

3.1 Material characterization

To investigate the morphology of the water spinach-derived porous carbons, field emission scanning electron microscopy (FESEM) and transmission electron microscopy (TEM) were carried out. It is noteworthy that the sample of WSAC-3

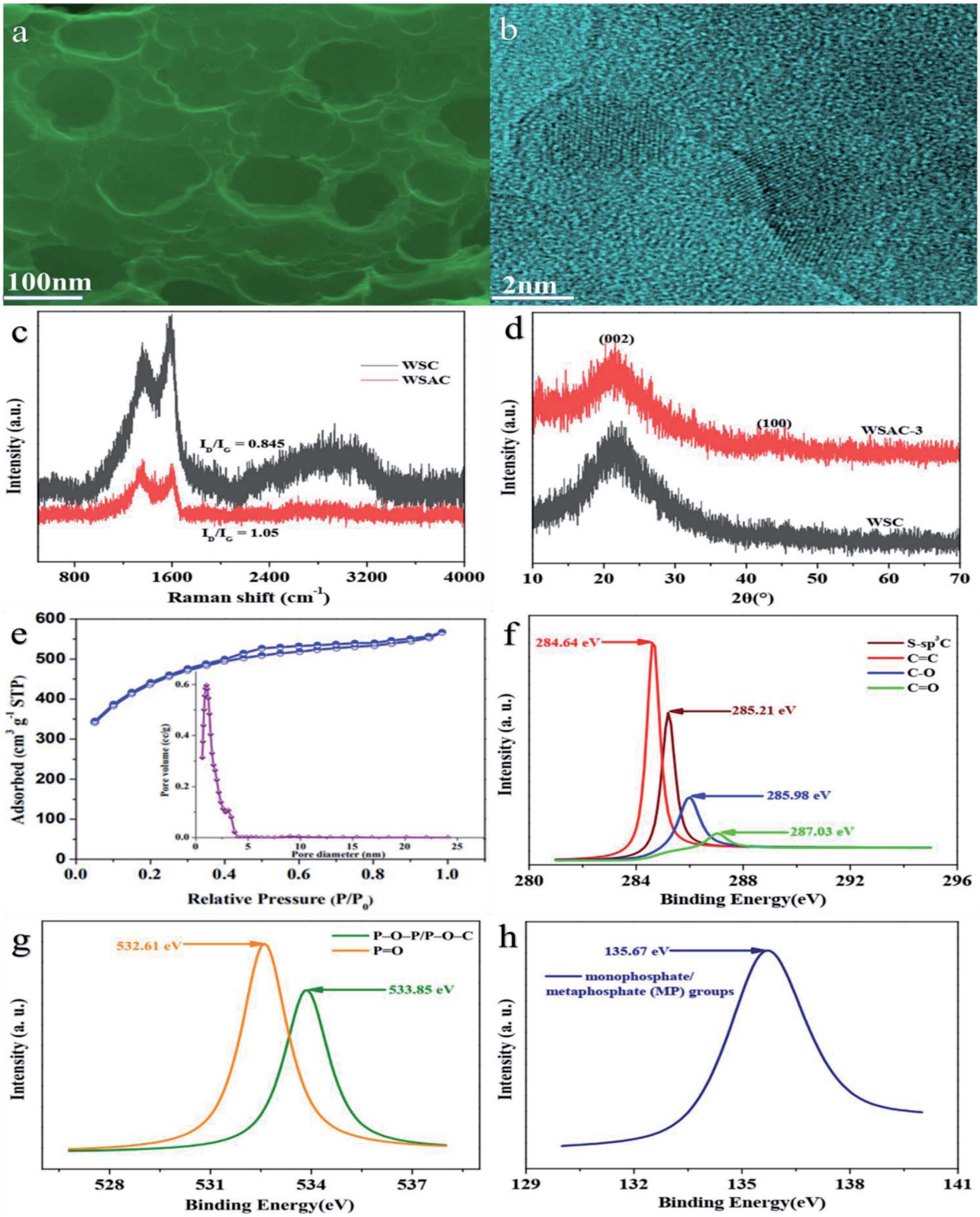

Fig. 1 (a) FESEM images of WSAC-3; (b) TEM images of WSAC-3; (c) XRD patterns of WSC and WSAC-3; (d) Raman spectra of WSC and WSAC-3; (e) N_2 adsorption/desorption isotherms and the pore size distribution of WSAC-3. (f) High resolution C 1s spectrum of WSAC-3. (g) High resolution O 1s spectrum of WSAC-3. (h) High resolution P 2p spectrum of WSAC-3.

indicates numerous irregular pores (Fig. 1a), which is ascribed to the activation of KOH. The activation procedure actually involves creating more pores and producing a highly porous solid phase for the carbon materials. Thus, plentiful pores are generated on the surface of the carbon materials. The unique pore structure can be favorable for efficient ion transfer, resulting in admirable supercapacitor performance.[25,26] As described in Fig. 1b, the typical TEM image with high resolution for WSAC-3 indicates a highly porous/nanostructured morphology and a homogeneous appearance with pores that are apparently in the mesopore range. The porous structure could contribute to inhibiting restacking and exposing more specific surface area, which further leads to shortening of the ion transmission path and acceleration of the reaction kinetics. According to Fig. 1c, there are two intensive absorbance regions at nearly 1320 cm^{-1} (D band) and 1590 cm^{-1} (G band), which refer to the defect disordered frameworks and tangential vibration of sp^2-hybridized carbon atoms, respectively.[27] The measured D, G band intensity ratio data (I_D/I_G) represents the graphitization degree. Simultaneously, the I_D/I_G ratio obviously increases from 0.845 for WSC to 1.05 for WSAC-3, which manifests that the activation of KOH could contribute to the generation of defective sites and could further enhance the electrochemical performance.[28] In Fig. 1e, it is obvious that two broad characteristic peaks at 2θ of 24.8° (graphitized carbon layer) and 41.6° (disordered carbon layer) can be seen, owing to the (002) and (100) planes of the graphitic carbon layers, respectively. This also confirms the presence of abundant amorphous defect sites.[29]

To further investigate the porosity of WSAC-3, N_2 adsorption/desorption isotherms analysis was conducted to explore the porous characteristics (Fig. 1e), and the relevant data are listed in Table 1. Type IV isotherms with H_4 hysteresis are attributed to the presence of micropores and mesopores, respectively.[30] The slight uptake tendency at relative pressures above 1.0 demonstrates the coexistence of macropores, which confirms the hierarchical micro-/meso-/macroporous structure for WSAC-3.[31] Additionally, the specific surface area of WSAC-3 was calculated to be ~1559 $m^2\ g^{-1}$, which is higher than that of WSC, with a specific surface area of ~209 $m^2\ g^{-1}$; this demonstrates that the activation of KOH could regulate the synthesis of porous carbon materials. Specifically, numerous micropores are generated on the carbon material due to the etching and intercalation effects of KOH.[32] With the formation of decomposition products, such as H_2O, CO, CO_2, and NH_3, during the pyrolysis process, the release of gasification molecules will open up closed pores, leading to the further development of pores to form meso-/macropores.[33] Simultaneously, the alkali metal K is intercalated into the carbon lattice, which contributes to the formation of large pores. After the metal residue is removed by hydrochloric acid washing, the pore volume is further increased, which greatly avoids the complicated preparation process. As expected, KOH has extremely good prospects to serve as a porogen to form a hierarchical porous structure for supercapacitors. The hierarchical pore structure can facilitate ion transport and provide sites for charge storage, which would be expected to exhibit favourable electrochemical performance for capacitor behavior.[34,35] Based on the DFT pore size distribution curves, the average pore sizes of WSAC-3 and WSC are 2.42 nm and 6.45 nm, respectively. The activation of KOH could lead to an increase of the textural properties and further maximization of the ion adsorption sites, owing to the generation of a substantial amount of gas (CO, and CO_2) from the activation agent (KOH).[36] In view of the effect of the activation temperature, the BET surface areas and the pore volumes as well as the average pore sizes of WSAC-6 (700 °C) and WSAC-8 (1000 °C) are 1024.35 $m^2\ g^{-1}$, 0.753 $cm^{-3}\ g^{-1}$, 3.572 nm and 957.36 $m^2\ g^{-1}$, 0.627 $cm^{-3}\ g^{-1}$, 3.672 nm, respectively. As the activation temperature varies from 700 °C to 900 °C, the textural properties similarly increase. Meanwhile, as the activation temperature further increases to 1000 °C, the pores may collapse, which leads to an unfavourable decrease of the textural properties.[37]

In-depth characterizations of the chemical element compositions of materials were performed by XPS measurements (Fig. S1†). Oxygen and phosphorus elements were introduced in the carbon skeleton of WSAC-3 *via* the pyrolysis strategy (Fig. S2†). The C atoms of WSAC-3 appear mainly to be C=C (284.64 eV), S–sp^3C (285.21 eV), C–O (285.98 eV) and C=O (287.03 eV) (Fig. 1f).[38] O atoms appear in the form of P=O (532.61 eV) and P–O–P/P–O–C (533.85 eV), (Fig. 1g).[39] P atoms manifest as monophosphate/metaphosphate (MP) groups

Table 1 Summary of the BET characteristics of the activated carbons

Sample	S_{BET}[a]	V_{tot}[b]	S_{mi}[c]	S_{me}[d]	S_{ma}[e]	V_{mi}[f]	V_{me}[g]	V_{ma}[h]
WSC	208.761	0.753	65.284	97.642	45.835	0.12	0.49	0.143
WSAC-1	1345.61	0.765	146.762	724.765	474.083	0.16	0.384	0.221
WSAC-2	1421.38	0.637	213.475	754.283	453.622	0.117	0.325	0.195
WSAC-3	1558.695	0.879	316.295	1013.742	228.658	0.164	0.417	0.298
WSAC-4	1527.35	0.618	108.613	1067.382	351.355	0.105	0.426	0.087
WSAC-5	1238.62	0.934	96.147	873.154	269.319	0.172	0.543	0.219
WSAC-6	1024.35	0.753	87.246	682.154	254.95	0.137	0.365	0.251
WSAC-7	1146.27	0.594	125.713	614.286	406.271	0.128	0.315	0.151
WSAC-8	957.36	0.627	96.217	763.258	97.885	0.136	0.425	0.066

[a] S_{BET}: BET surface area. [b] V_{tot}: total volume. [c] S_{mi}: micropore surface area. [d] S_{me}: mesopore surface area. [e] S_{ma}: macropore surface area. [f] V_{mi}: micropore volume. [g] V_{me}: mesopore volume. [h] V_{ma}: macropore volume.

(135.67 eV) (Fig. 1h).[40] Moreover, owing to the hydrophilicity of the O-containing groups, the O groups in WSAC-3 promote the wettability of the electrolyte interface, further enhancing the electrochemical performance. For comparison, the XPS spectrum of WSC also confirms the presence of C, O, and P (Fig. S3†). The high-resolution XPS C 1s spectrum (Fig. S4a†) is deconvoluted into four components at 284.7 eV, 285 eV, 291.2 eV, and 293.1 eV, which are assigned to C=C, S-sp^{3}C, C=O/O–C=O, and π–π*, respectively.[38] On account of the O 1s spectra (Fig. S4b†), two peaks at 531.5 eV and 532.7 eV are

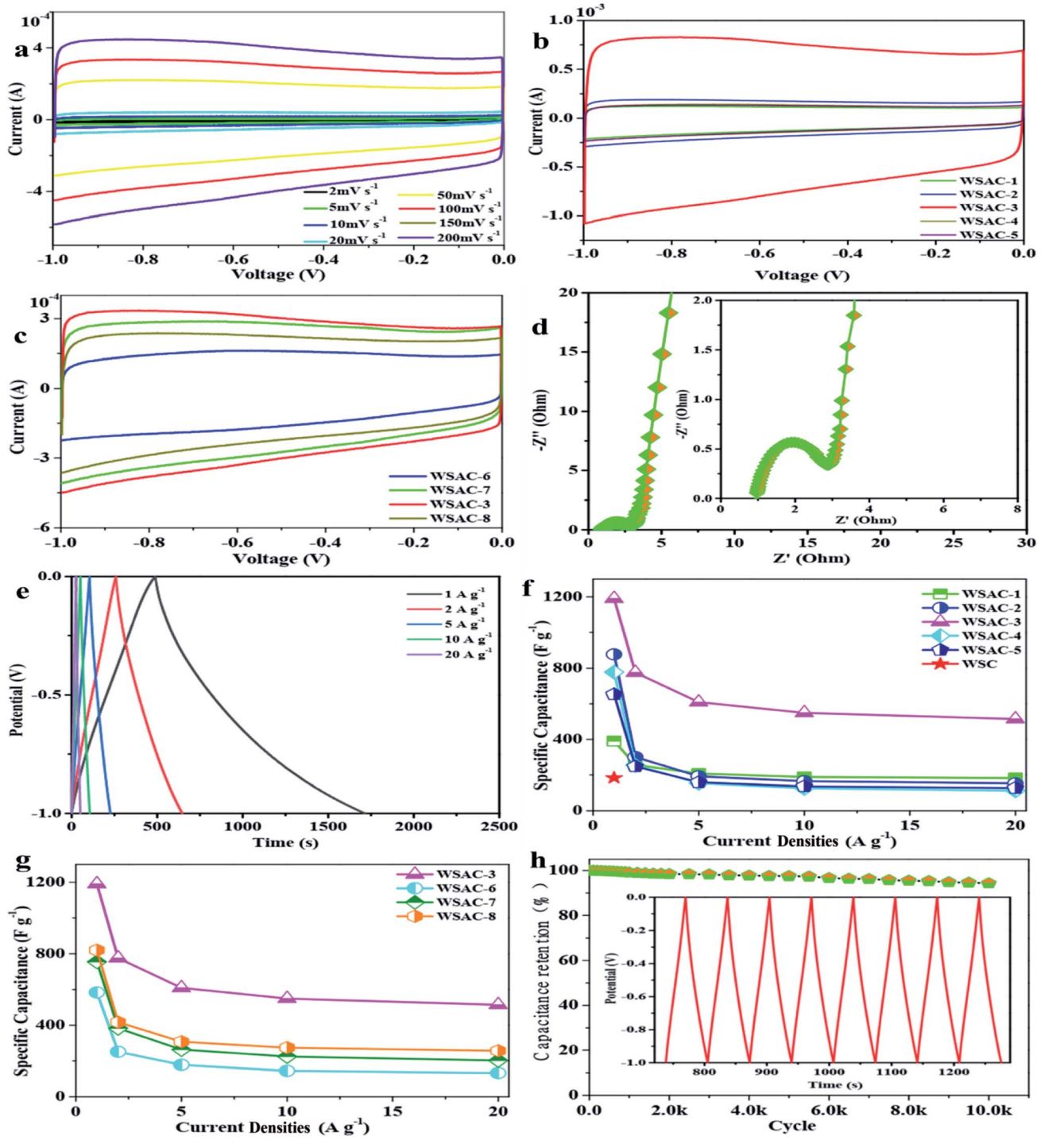

Fig. 2 (a) CV curves of WSAC-3 at different scan rates. (b) CV curves of WSAC samples prepared with different ratios of precursor/KOH at 100 mV s^{-1}. (c) CV curves of WSAC samples prepared under different temperatures at 100 mV s^{-1}. (d) Nyquist plots of PSAC-3. (e) Galvanostatic charge/discharge curves of WSAC-3 at different current densities. (f) Capacitances of WSAC samples prepared with different ratios of precursor/KOH at different current densities. (g) Capacitances of WSAC samples prepared under different temperatures at different current densities. (h) Cycling performance of WSAC-3 at 10 A g^{-1}. The inset shows the GCD curves for 10 000 cycles.

attributed to P=O groups and P–O–P/P–O–C linkages, respectively.[39] According to the P 2p spectra, the three peaks at 132.9 eV, 133.4 eV and 134.5 eV can be assigned to C–P species (Fig. S4c†), pyrophosphate/polyphosphate (PP) and monophosphate/metaphosphate (MP) groups, respectively.[40] These element composition results are consistent with the FTIR spectra. According to the FTIR spectra in Fig. S5,† the characteristic peaks at around 3747, 2924, 2328, 1660, and 1047 cm^{-1} are designated as the vibrations of O–H, sp^3C–H, C–O, C=O, and C–O–C, respectively.[41]

3.2 Electrochemical behavior of the electrode

To further investigate and analyse the electrochemical characteristics of the porous carbon materials, measurements such as CV, GCD and EIS were carried out. As described in Fig. 2a, WSAC-3 indicates relatively quasi-rectangular curves even at a sweep rate of 200 mV s^{-1}, which confirms the excellent capacitor performance.[42] This is mainly attributed to the pore structure and the larger micropore area, as well as to the relatively short diffusion distance of the dielectric ions from the mesopores to the micropores.[43] Meanwhile, a couple of reversible humps could also be observed, owing not only to the electric double layer formation but also the faradaic redox reactions correlated with O/P-containing functional groups.[44] As shown in Fig. 2b and c, the CV curves retained their symmetrically rectangular nature, which demonstrates that all the carbon materials manifest good capacitor behaviour and further contribute to the rapid ion spread within the hierarchical pore structure along with the low diffusion resistance.[45] Moreover, WSAC-3 exhibits the largest enclosed integral area among the as-obtained carbon materials.

Based on the kinetics information related to the electron/ion transport process and the electrochemical properties, EIS investigations were carried out to evaluate the resistance and the capacitive performance of the materials. As shown in Fig. 2d, the nearly vertical line in the low frequency region presents the diffuse resistance; also, the semicircle in the high frequency region is related to the charge transmission resistance.[46] The enlarged Nyquist plot for WSAC-3 obviously indicates the interface of the carbon material and stainless steel grid. The semicircle represents the charge transmission resistance (R_{ct}) at the interface of the electrolyte and materials, which corresponds to the electric double layer and faradaic redox reaction at the interface.[47] WSAC-3 exhibits low total resistance values (0.9 Ω), which suggests a high charge transfer transition, ion penetration, electroconductivity, and a rapid ion diffusion rate; further, it could contribute to the electrical double-layer capacitance.[48] This high supercapacitor performance of WSAC-3 is highly related to its hierarchical micro-/meso-/macroporous structure, which is beneficial to charge adsorption and aggregation.[49]

GCD measurements were conducted in the current density range from 1 A g^{-1} to 20 A g^{-1} (Fig. 2e). The GCD curves for WSAC-3 present an isosceles triangle with slight distortion and no obvious IR drop even at a high current. The specific capacitance of WSAC-3 could be achieved as ~1191 F g^{-1} at 1 A g^{-1}, which is much higher than that of WSC (~183 F g^{-1} at 1 A g^{-1}) by virtue of the activation of KOH and is remarkable for biomass-carbonaceous electrode materials.[50–52] Meanwhile, a capacitance of ~330 F g^{-1} could still be reached even at 20 A g^{-1}, which presents excellent attractive capacitor behavior and rate capability.[53] The lowered capacitance at higher current densities is owing to the short diffusion duration for the migration of K^+/H^+ ions in the electrolyte at the active site of the electrode surface at a rapid rate under high current.[54] Accompanied with the increased ratio of KOH/WSC (Fig. 2f), the specific capacitance increases until it reaches an optimum value, beyond which it drastically decreases again. According to Fig. 2f, it is obvious that the specific capacitances of the WSAC samples increase with the decrease of the ratio of WSC to KOH (2 : 1 *vs.* 3 : 2 *vs.* 1 : 1, 390.03 *vs.* 878 *vs.* 1190.59 F g^{-1} at 1 A g^{-1}; WSAC-1 *vs.* WSAC-2 *vs.* WSAC-3). However, the specific capacitances for the WSAC samples also progressively decrease along with the decrease of the ratio of WSC/KOH (1 : 1 *vs.* 2 : 3 *vs.* 1 : 2, 1190.59 *vs.* 778.54 *vs.* 653.26 F g^{-1}, WSAC-3 *vs.* WSAC-4 *vs.* WSAC-5). Apart from this, the specific capacitance of WSAC-3 at 800 °C (Fig. 2g) obviously exceeded that of WSAC-6 (600 °C) and WSAC-7 (700 °C) as well as WSAC-8 (900 °C) (800 *vs.* 600 *vs.* 700 *vs.* 900 °C, 1190.59 *vs.* 583.42 *vs.* 755.46 *vs.* 820.71 F g^{-1} at 1 A g^{-1}; WSAC-4 *vs.* WSAC-6 *vs.* WSAC-7 *vs.* WSAC-8), owing to the formation of a broader continuous 3D porous framework, which contributes to efficient infiltration of the electrolyte and fast transport of ions as well as efficient current collection.[55] WSAC-3 indicates outstanding supercapacitor performance owing to its appropriate pore volume, broadened pore-size distribution, ultrahigh specific surface area, and well-developed hierarchical pore structure by the activation of KOH.[56] Notably, the active method could introduce various kinds of pores into the material effectively and efficiently, which only involved a facile synthetic procedure. A suitable pore distribution could not only avoid the need for long, complicated channels for efficient charge storage and aggregation, but also could provide sufficient storage sites for charges and ions (Fig. 3). Moreover, the presence of oxygen/phosphorus doping could contribute to the electric conductivity and wettability of the active carbon material, which further improves the ion transfer efficiency and capacity.[57,58]

The stability of WSAC-3 was investigated by charging and discharging at 10 A g^{-1} for 10 000 cycles. On account of the specific capacitance *versus* the number of cycles in Fig. 2h, it is obvious that excellent cycling stability with 94.3% retention of the initial capacitance is indicated. The real-time capacitance

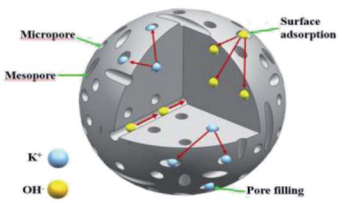

Fig. 3 Schematic representation of the porous structure and electrolyte ion storage in WASC-3.

value slightly exceeds the initial capacitance value during cycling. The decreasing trend of capacitance could be ascribed to the blocking of the electrode surface (pores and channels) by the electrolyte.[59] Notably, the GCD curve of the 1300th cycle retains an almost identical shape to the 1st cycle by maintaining its linearity and symmetry, highlighting the excellent reversibility and long-term electrochemical stability (inset in Fig. 2h).

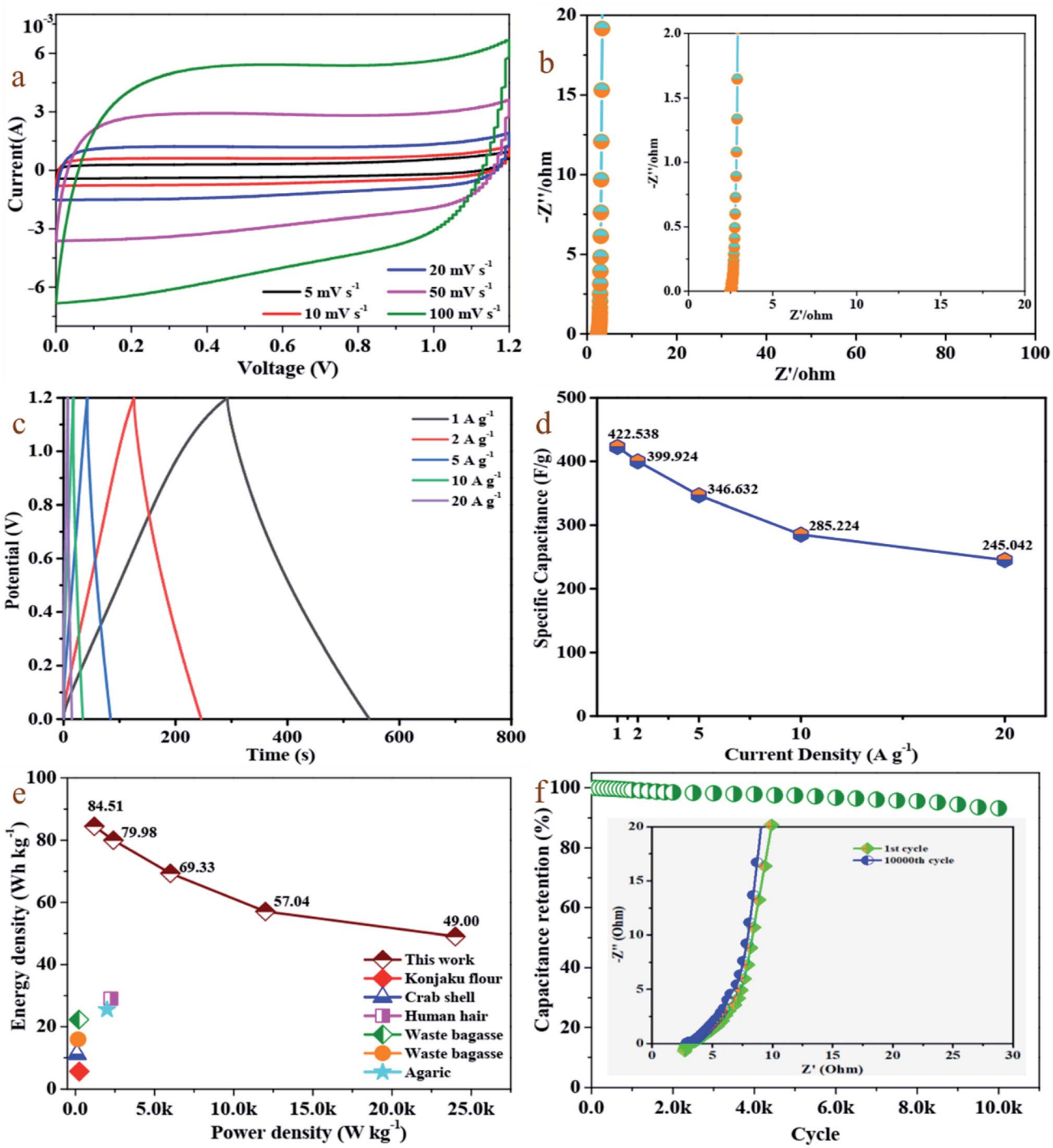

Fig. 4 (a) CV curves of the WSAC//WSAC symmetrical supercapacitor at different scan rates in the voltage window of 0–1.2 V. (b) Nyquist plots of the PSAC//PSAC symmetrical supercapacitor. (c) Galvanostatic charge/discharge curves of the WSAC//WSAC symmetrical supercapacitor at different current densities. (d) Specific capacitances of the as-assembled WSAC symmetrical supercapacitor based on the total mass of the active materials of the two electrodes at different current densities. (e) Ragone plots of the WSAC symmetrical supercapacitor and other previously reported carbon-based symmetric supercapacitors. (f) Cycle performance of the WSAC symmetrical supercapacitor at 10 A g^{-1} (inset: the Nyquist plots for recycling).

There results demonstrate the remarkably high long-term cycling stability and rate capability of the WSAC electrode.

3.3 Supercapacitor performance

As described in Fig. 4a, the CV curves at different scan rates varying from 2 to 100 mV s^{-1} indicate an approximately rectangular shape with slight faradaic humps, which confirms the combination of double-layer capacitive and pseudocapacitive behavior caused by the existence of active oxygen and phosphorous heteroatoms.[60] While the current density increases along with the scan rate, the CV profiles still retain a near-rectangle shape at various scan rates, which demonstrates the excellent capacitive and behavior rate performance as well as the faster kinetics in the porous carbon due to the openness in its structure, which favors fast ion transportation inside the pores.[61] At 100 mV s^{-1}, the CV curves still manifest the EDLC shape along with a large output current, owing to an increase in ion transport and ion adsorption kinetics after hetero atom doping.[62]

The Nyquist plots of the device (Fig. 4b) manifest an initial solution resistance, a semi-circle in the high-frequency region that can be attributed to charge transfer resistance originating from the electronic and ionic conductivity of the carbon electrode, and a Warburg tail at low frequency, indicating capacitive-type storage. The small semicircle of the device indicates good ionic conductivity by virtue of the high degree of graphitization, which contributes to the high electrical conductivity of electrode materials. An almost vertical-line feature in the low-frequency region indicates nearly ideal capacitive behavior and low diffusion resistance of electrolyte ions in the electrode material. The supercapacitor also exhibits a low intercept (2.49 Ω) on the real axis owing to the surface wettability derived from the coexistence of P and O.[63]

The charge–discharge (CD) curves (Fig. 4c) manifest a highly symmetrical and linear triangular shape profile, confirming the pure double-charge storage reaction in capacitors,[64] which is consistent with the CV results mentioned above. Fig. 4d compares the capacitance of the device in a range of current densities from 1 to 10 A g^{-1} accompanied with the change of capacitance from ~423 to ~285 F g^{-1}. Even at a relatively high current density of 20 A g^{-1}, the specific capacitance is still maintained at ~245 F g^{-1}, revealing good rate capability and low CT resistance, which are promising features for high-performing SCs.[65] Generally, the excellent rate capacity of the device is closely associated with the low polarization effects of the electrodes, which is governed by the high electron conductivity of the electrodes and rapid electrolyte diffusion. Moreover, the presence of dual hetero atoms of O and P greatly reduces this resistance and increases the pore utilization to achieve a high capacitance.[66]

Based on the Ragone plot of the device calculated from discharge curves at different current densities (Fig. 4e), the capacitor delivers a high energy density of ~84.51 W h kg^{-1} at a power density of 1.2 kW kg^{-1} and maintains 49 W h kg^{-1} at a high power density of 24 kW kg^{-1}, which is higher than those of commercially available supercapacitors (3–5 W h kg^{-1}) and other previously reported biomass-derived heteroatom-doped carbonaceous symmetric supercapacitors. This high power capability matches well with the remarkable rate performance and excellent capacitance retention of the device. Moreover, the capacitive performance can be ascribed to the rational pore structure of the active materials and the synergistic role of the two symmetric electrodes.[67]

Long-term cyclic stability is one of the important factors of supercapacitors for practical use. The cycling stability of this supercapacitor was measured at a current density of 10 A g^{-1} within an operating voltage range from 0 to 1.2 V (Fig. 4f). The symmetric capacitor indicates superior cycling stability with 93.2% of the initial capacitance retention after 10 000 cycles, which is attributed to the robust structure and high surface area of these water spinach-derived porous carbons as well as their short ion diffusion lengths for energy storage.[68] Notably, the Nyquist plots (shown in the inset of Fig. 4f) are almost fully overlapped except for a faint decay in the plateau current for the latter after 10 000 cycles, further evidencing the excellent cycling stability of the supercapacitor.[69,70] To further explore the practical requirements for portable and wearable electronics applications, a tandem device was assembled by connecting two prototype units in series. Then, the device was applied to light up a red light-emitting-diode (LED; the lowest working potential is 2.0 V), as depicted in the inset of Fig. S6.† This tentative test confirms that the facile and cost-efficient synthesis strategy for designing analogous biomass-derived materials such as WSAC-3 paves the way for a new direction for expanding their practical applications in energy storage and conversion.

4. Conclusions

In summary, a hierarchically porous structured carbon material was fabricated in a facile way by pyrolyzing KOH as a porogen and water spinach biomass as a carbon source along with HCl etching. The as-synthesized product with a rough surface could increase the number of active sites and facilitate the ion transport of the electrolyte, thereby resulting in superior specific capacitance. In addition, the as-assembled symmetric device based on WSAC delivered superior electrochemical characteristics, such as capacitance (~423 F g^{-1} at 1 A g^{-1}), rate capability, energy densities (~84.51 W h kg^{-1} at a power density of 1.2 kW kg^{-1}) and cycling performance (only 6.8% capacitance loss after 10 000 cycles). In principle, the doped hierarchical porous carbon from biomass could be employed in a wide range of applications, such as batteries, fuel cells, water treatment and catalysis.

Conflicts of interest

There are no conflicts to declare.

Acknowledgements

We gratefully acknowledge to the financial support from Faculty of Materials and Energy and Institute for Clean Energy & Advanced Materials, Southwest University and Chongqing Key

Laboratory for Advanced Materials and Technologies of Clean Electrical Power Sources and sponsored by Natural Science Foundation of Chongqing, China (cstc2020jcyj-msxmX0019).

References

1 W. Yang, W. Yang, L. Kong, A. Song, X. J. Qin and G. J. Shao, *Carbon*, 2018, **127**, 557.
2 Z. Li, K. Ahadi, K. Jiang, B. Ahvazi, P. Li, A. O. Anyia, K. Cadien and T. Thundat, *Nano Res.*, 2017, **10**, 1847.
3 L. W. Ji, P. Meduri, V. Agubra, X. C. Xiao and M. Alcoutlabi, *Adv. Energy Mater.*, 2016, **6**, 1502159.
4 B. Zhang, F. Kang, J. M. Tarascon and J. K. Kim, *Prog. Mater. Sci.*, 2016, **76**, 319.
5 W. B. Kong, L. J. Yan, Y. F. Luo, D. T. Wang, K. L. Jiang, Q. Q. Li, S. S. Fan and J. P. Wang, *Adv. Funct. Mater.*, 2017, **27**, 1606663.
6 R. Raccichini, A. Varzi, D. Wei and S. Passerini, *Adv. Mater.*, 2017, **29**, 1603421.
7 Y. R. Liu, Y. Nie, X. M. Lu, X. P. Zhang, H. Y. He, F. J. Pan, L. Zhou, X. Liu, X. Y. Ji and S. J. Zhang, *Green Chem.*, 2019, **21**, 3499.
8 M. Genovese, J. H. Jiang, K. Lian and N. Holm, *J. Mater. Chem. A*, 2015, **3**, 2903.
9 L. Wei, M. Sevilla, A. B. Fuertes, R. Mokaya and G. Yushin, *Adv. Energy Mater.*, 2011, **1**, 356.
10 Z. J. Li, W. Lv, C. Zhang, B. H. Li, F. Y. Kang and Q. H. Yang, *Carbon*, 2015, **92**, 11.
11 M. Genovese and K. Lian, *J. Mater. Chem. A*, 2017, **5**, 3939.
12 K. Tekin, S. Karagöz and S. Bektaş, *Renewable Sustainable Energy Rev.*, 2014, **40**, 673.
13 J. C. Wang and S. Kaskel, *J. Mater. Chem.*, 2012, **22**, 23710.
14 V. Subramanian, C. Luo, A. M. Stephan, K. S. Nahm, S. Thomas and B. Q. Wei, *J. Phys. Chem. C*, 2007, **111**, 7527.
15 V. Selvamani, R. Ravikumar, V. Suryanarayanan, D. Velayutham and S. Gopukumar, *Electrochim. Acta*, 2015, **182**, 1.
16 Z. H. Wang, D. K. Shen, C. F. Wu and S. Gu, *Green Chem.*, 2018, **20**, 5031.
17 Y. Bai, C. L. Liu, T. T. Chen, W. T. Li, S. S. Zheng, Y. C. Pi, Y. S. Luo and H. Pang, *Angew. Chem., Int. Ed.*, 2021, **133**, 25522.
18 S. S. Zheng, Y. Ru, H. G. Xue and H. Pang, *Chin. Chem. Lett.*, 2021, **32**(12), 3817–3820.
19 Q. L. Wu, X. C. Yan, Y. Jia and X. D. Yao, *EnergyChem*, 2021, **3**, 100059.
20 Y. Yuan, Y. J. Yang and G. S. Zhu, *EnergyChem*, 2020, **2**, 100037.
21 J. Wang, P. Nie, B. Ding, S. Y. Dong, X. D. Hao, H. Dou and X. G. Zhang, *J. Mater. Chem. A*, 2017, **5**, 2411.
22 F. X. Wang, X. W. Wu, X. H. Yuan, Z. C. Liu, Y. Zhang, L. J. Fu, Y. S. Zhu, Q. M. Zhou, Y. P. Wu and W. Huang, *Chem. Soc. Rev.*, 2017, **46**, 6816.
23 X. Zhou, P. L. Wang, Y. G. Zhang, L. L. Wang, L. T. Zhang, L. Zhang, L. Xu and L. Liu, *J. Mater. Chem. A*, 2017, **5**, 12958.
24 B. Li, F. Dai, Q. F. Xiao, L. Yang, J. M. Shen, C. M. Zhang and M. Cai, *Energy Environ. Sci.*, 2016, **9**, 102.
25 Z. H. Bi, Q. Q. Kong, Y. F. Cao, G. H. Sun, F. Y. Su, X. X. Wei, X. M. Li, A. Ahmad, L. J. Xie and C. M. Chen, *J. Mater. Chem. A*, 2019, **7**, 16028.
26 N. Choudhary, C. Li, J. L. Moore, N. Nagaiah, L. Zhai, Y. Jung and J. Thomas, *Adv. Mater.*, 2017, **29**, 1605336.
27 Z. Y. Miao, Y. Huang, J. P. Xin, X. W. Su, Y. H. Sang, H. Liu and J. J. Wang, *ACS Appl. Mater. Interfaces*, 2019, **11**, 18044.
28 G. K. Veerasubramani, A. Chandrasekhar, M. S. P. Sudhakaran, Y. S. Mok and S. J. Kim, *J. Mater. Chem. A*, 2017, **5**, 11100.
29 Z. J. Li, W. Lv, C. Zhang, B. H. Li, F. Y. Kang and Q. H. Yang, *Carbon*, 2015, **92**, 11.
30 M. L. Li, H. Y. Xiao, T. Zhang, Q. R. Li and Y. F. Zhao, *ACS Sustainable Chem. Eng.*, 2019, **7**, 4716.
31 W. S. Chen, H. P. Yu, S. Y. Lee, T. Wei, J. Lia and Z. J. Fan, *Chem. Soc. Rev.*, 2018, **47**, 2837.
32 W. Du, X. N. Wang, X. Q. Sun, J. Zhan, H. D. Zhang and X. J. Zhao, *J. Electroanal. Chem.*, 2018, **827**, 213.
33 J. W. Liu, S. X. Min, F. Wang and Z. G. Zhang, *J. Power Sources*, 2020, **466**, 228347.
34 M. Sevilla, N. Diez, G. A. Ferrero and A. B. Fuertes, *Energy Storage Mater.*, 2019, **18**, 356.
35 G. Laura, S. F. Loreto, Q. M. Nausika, V. Viliam, K. Peter, S. Viera and Á. C. Teresa, *Electrochim. Acta*, 2019, **298**, 910.
36 J. L. Goldfarb, G. L. Dou, M. Salari and M. W. Grinstaff, *ACS Sustainable Chem. Eng.*, 2017, **5**, 3046.
37 A. Borenstein, O. Hanna, R. Attias, S. Luski, T. Broussebc and D. Aurbach, *J. Mater. Chem. A*, 2017, **5**, 12653.
38 A. Sugahara, Y. Ando, S. Kajiyama, K. Yazawa, K. Gotoh, M. Otani, M. Okubo and A. Yamada, *Nat. Commun.*, 2019, **10**, 850.
39 A. Noori, M. F. E. Kady, M. S. Rahmanifar, R. B. Kaner and M. F. Mousavi, *Chem. Soc. Rev.*, 2019, **48**, 1272.
40 K. F. Chen, S. Y. Song, F. Liu and D. F. Xue, *Chem. Soc. Rev.*, 2015, **44**, 6230.
41 G. P. Wang, L. Zhang and J. J. Zhang, *Chem. Soc. Rev.*, 2012, **41**, 797.
42 J. Niu, R. Shao, J. J. Liang, M. L. Dou, Z. L. Li, Y. Q. Huang and F. Wang, *Nano Energy*, 2017, **36**, 322.
43 M. J. Yuan, X. T. Guo, Y. Liu and H. Pang, *J. Mater. Chem. A*, 2019, **7**, 22123.
44 W. J. Liu, H. Jiang and H. Q. Yu, *Energy Environ. Sci.*, 2019, **12**, 1751.
45 Y. Q. Zhang, X. Liu, S. L. Wang, L. Li and S. X. Dou, *Adv. Energy Mater.*, 2017, **7**, 1700592.
46 C. J. Wang, D. P. Wu, H. J. Wang, Z. Y. Gao, F. Xu and K. Jiang, *J. Mater. Chem. A*, 2018, **6**, 1244.
47 W. Liu, Y. Cui, X. Du, Z. Zhang, Z. S. Chao and Y. L. Deng, *Energy Environ. Sci.*, 2016, **9**, 467.
48 B. J. Zhu, B. Liu, C. Qu, H. Zhang, W. H. Guo, Z. B. Liang, F. Chen and R. Q. Zou, *J. Mater. Chem. A*, 2018, **6**, 1523.
49 Z. H. Bi, Q. Q. Kong, Y. F. Cao, G. H. Sun, F. Y. Su, X. X. Wei, X. M. Li, A. Ahmad, L. J. Xie and C. M. Chen, *J. Mater. Chem. A*, 2019, **7**, 16028.
50 R. W. Mo, F. Li, X. Y. Tan, P. C. Xu, R. Tao, G. R. Shen, X. Lu, F. Liu, L. Shen, B. Xu, Q. F. Xiao, X. Wang, C. M. Wang, J. L. Li, G. Wang and Y. F. Lu, *Nat. Commun.*, 2019, **10**, 1474.

51 W. J. Qian, F. X. Sun, Y. H. Xu, L. H. Qiu, C. H. Liu, S. D. Wang and F. Yan, *Energy Environ. Sci.*, 2014, **7**, 379.
52 Q. Zhang, K. H. Han, S. J. Li, M. Li, J. X. Li and K. Ren, *Nanoscale*, 2018, **10**, 2427.
53 J. M. Sun, Z. W. Wu, C. H. Ma, M. C. Xu, S. Luo, W. Li and S. X. Liu, *J. Mater. Chem. A*, 2021, **9**, 13822.
54 C. J. Chen, Y. D. Kuang, S. Z. Zhu, I. Burgert, T. Keplinger, A. Gong, T. Li, L. Berglund, S. J. Eichhorn and L. B. Hu, *Nat. Rev. Mater.*, 2020, **5**, 642.
55 W. G. Cui, T. L. Hu and X. H. Bu, *Adv. Mater.*, 2020, **32**, 1806445.
56 F. Guo, Y. P. Wei, S. Q. Wang, X. Y. Zhang, F. M. Wang and W. Y. Sun, *J. Mater. Chem. A*, 2019, **7**, 26490.
57 A. G. Martin, J. M. Fernandez, M. Ruttert, M. Winter, T. Placke and J. R. Rico, *Carbon*, 2020, **164**, 261.
58 M. A. A. M. Abdah, N. H. N. Azman, S. Kulandaivalu, N. A. Rahman, A. H. Abdullah and Y. Sulaiman, *J. Power Sources*, 2019, **44**, 227324.
59 L. Qiu, Z. J. He and D. Li, *Adv. Mater.*, 2018, **30**, 1704850.
60 M. Dasbach, M. Pyschik, V. Lehmann, K. Parey, D. Rhinow, H. M. Reinhardt and N. A. Hampp, *ACS Nano*, 2020, **14**, 8181.
61 H. Wan, M. H. Lv, X. H. Liu, G. Chen, N. Zhang, Y. J. Cao, H. D. Wang, R. Z. Ma and G. Z. Qiu, *ACS Sustainable Chem. Eng.*, 2019, **7**, 18819.
62 L. A. Berglund and I. Burgert, *Adv. Mater.*, 2018, **30**, 1704285.
63 M. W. Zhu, Y. J. Li, G. Chen, F. Jiang, Z. Yang, X. G. Luo, Y. B. Wang, S. D. Lacey, J. Q. Dai, C. W. Wang, C. Jia, J. Y. Wan, Y. G. Yao, A. Gong, B. Yang, Z. F. Yu, S. Das and L. B. Hu, *Adv. Mater.*, 2017, **29**, 1704107.
64 H. Xu, L. Y. Wang, Y. Zhang, Y. Chen and S. Y. Gao, *Nanoscale*, 2021, **13**, 10051.
65 Y. Guan, L. Yu and X. W. Lou, *J. Am. Chem. Soc.*, 2016, **138**, 11306.
66 Y. J. Fang, D. Y. Luan and X. W. Lou, *Adv. Mater.*, 2020, **32**, 2002976.
67 X. G. Li, B. Y. Guan, S. Y. Gao and X. W. Lou, *Energy Environ. Sci.*, 2019, **12**, 648.
68 L. Hao, J. Ning, B. Luo, B. Wang, Y. B. Zhang, Z. H. Tang, J. H. Yang, A. Thomas and L. J. Zhi, *J. Am. Chem. Soc.*, 2015, **137**, 219.
69 Y. Lu, J. N. Liang, S. F. Deng, Q. M. He, S. Y. Deng, Y. Z. Hu and D. L. Wang, *Nano Energy*, 2019, **65**, 103993.
70 S. Y. Gao, X. G. Li, L. Y. Li and X. J. Wei, *Nano Energy*, 2017, **33**, 334.